



# A Search for Neutrino Emission from Fast Radio Bursts with Six Years of IceCube Data

M. G. Aartsen<sup>1</sup>, M. Ackermann<sup>2</sup>, J. Adams<sup>1</sup>, J. A. Aguilar<sup>3</sup>, M. Ahlers<sup>4</sup>, M. Ahrens<sup>5</sup>, I. Al Samarai<sup>6</sup>, D. Altmann<sup>7</sup>, K. Andeen<sup>8</sup>, T. Anderson<sup>9</sup>, I. Ansseau<sup>3</sup>, G. Anton<sup>7</sup>, C. Argüelles<sup>10</sup>, J. Auffenberg<sup>11</sup>, S. Axani<sup>10</sup>, H. Bagherpour<sup>1</sup>, X. Bai<sup>12</sup>, J. P. Barron<sup>13</sup>, S. W. Barwick<sup>14</sup>, V. Baum<sup>15</sup>, R. Bay<sup>16</sup>, J. J. Beatty<sup>17,18</sup>, J. Becker Tjus<sup>19</sup>, K.-H. Becker<sup>20</sup>, S. BenZvi<sup>21</sup>, D. Berley<sup>22</sup>, E. Bernardini<sup>2</sup>, D. Z. Besson<sup>23</sup>, G. Binder<sup>24,16</sup>, D. Bindig<sup>20</sup>, E. Blaufuss<sup>22</sup>, S. Blot<sup>2</sup>, C. Bohm<sup>5</sup>, M. Börner<sup>25</sup>, F. Bos<sup>19</sup>, S. Böser<sup>15</sup>, O. Botner<sup>26</sup>, E. Bourbeau<sup>4</sup>, J. Bourbeau<sup>27</sup>, F. Bradascio<sup>2</sup>, J. Braun<sup>27</sup>, M. Brenzke<sup>11</sup>, H.-P. Bretz<sup>2</sup>, S. Bron<sup>6</sup>, J. Brostean-Kaiser<sup>2</sup>, A. Burgman<sup>26</sup>, R. S. Busse<sup>27</sup>, T. Carver<sup>6</sup>, E. Cheung<sup>22</sup>, D. Chirkin<sup>27</sup>, A. Christov<sup>6</sup>, K. Clark<sup>28</sup>, L. Classen<sup>29</sup>, G. H. Collin<sup>10</sup>, J. M. Conrad<sup>10</sup>, P. Coppin<sup>30</sup>, P. Correa<sup>30</sup>, D. F. Cowen<sup>9,31</sup>, R. Cross<sup>21</sup>, P. Dave<sup>32</sup>, M. Day<sup>27</sup>, J. P. A. M. de André<sup>33</sup>, C. De Clercq<sup>30</sup>, J. J. DeLaunay<sup>9</sup>, H. Dembinski<sup>34</sup>, S. De Ridder<sup>35</sup>, P. Desiati<sup>27</sup>, K. D. de Vries<sup>30</sup>, G. de Wasseige<sup>30</sup>, M. de With<sup>36</sup>, T. DeYoung<sup>33</sup>, J. C. Díaz-Vélez<sup>27</sup>, V. di Lorenzo<sup>15</sup>, H. Dujmovic<sup>37</sup>, J. P. Dumm<sup>5</sup>, M. Dunkman<sup>9</sup>, E. Dvorak<sup>12</sup>, B. Eberhardt<sup>15</sup>, T. Ehrhardt<sup>15</sup>, B. Eichmann<sup>19</sup>, P. Eller<sup>9</sup>, P. A. Evenson<sup>34</sup>, S. Fahey<sup>27</sup>, A. R. Fazely<sup>38</sup>, J. Felde<sup>22</sup>, K. Filimonov<sup>16</sup>, C. Finley<sup>5</sup>, S. Flis<sup>5</sup>, A. Franckowiak<sup>2</sup>, E. Friedman<sup>22</sup>, A. Fritz<sup>15</sup>, T. K. Gaisser<sup>34</sup>, J. Gallagher<sup>39</sup>, L. Gerhardt<sup>24</sup>, K. Ghorbani<sup>27</sup>, W. Giang<sup>13</sup>, T. Glauch<sup>40</sup>, T. Glüsenkamp<sup>7</sup>, A. Goldschmidt<sup>24</sup>, J. G. Gonzalez<sup>34</sup>, D. Grant<sup>13</sup>, Z. Griffith<sup>27</sup>, C. Haack<sup>11</sup>, A. Hallgren<sup>26</sup>, F. Halzen<sup>27</sup>, K. Hanson<sup>27</sup>, D. Hebecker<sup>36</sup>, D. Heereman<sup>3</sup>, K. Helbing<sup>20</sup>, R. Hellauer<sup>22</sup>, S. Hickford<sup>20</sup>, J. Hignight<sup>33</sup>, G. C. Hill<sup>41</sup>, K. D. Hoffman<sup>22</sup>, R. Hoffmann<sup>20</sup>, T. Hoinka<sup>25</sup>, B. Hokanson-Fasig<sup>27</sup>, K. Hoshina<sup>27,42</sup>, F. Huang<sup>9</sup>, M. Huber<sup>40</sup>, K. Hultqvist<sup>5</sup>, M. Hünnefeld<sup>25</sup>, R. Hussain<sup>27</sup>, S. In<sup>37</sup>, N. Iovine<sup>3</sup>, A. Ishihara<sup>43</sup>, E. Jacobi<sup>2</sup>, G. S. Japaridze<sup>44</sup>, M. Jeong<sup>37</sup>, K. Jero<sup>27</sup>, B. J. P. Jones<sup>45</sup>, P. Kalaczynski<sup>11</sup>, W. Kang<sup>37</sup>, A. Kappes<sup>29</sup>, D. Kappesser<sup>15</sup>, T. Karg<sup>2</sup>, A. Karle<sup>27</sup>, U. Katz<sup>7</sup>, M. Kauer<sup>27</sup>, A. Keivani<sup>9</sup>, J. L. Kelley<sup>27</sup>, A. Kheirandish<sup>27</sup>, J. Kim<sup>37</sup>, M. Kim<sup>43</sup>, T. Kintscher<sup>2</sup>, J. Kiryluk<sup>46</sup>, T. Kittler<sup>7</sup>, S. R. Klein<sup>24,16</sup>, R. Koirala<sup>34</sup>, H. Kolanoski<sup>36</sup>, L. Köpke<sup>15</sup>, C. Kopper<sup>13</sup>, S. Kopper<sup>47</sup>, J. P. Koschinsky<sup>11</sup>, D. J. Koskinen<sup>4</sup>, M. Kowalski<sup>2,36</sup>, K. Krings<sup>40</sup>, M. Kroll<sup>19</sup>, G. Krückl<sup>15</sup>, S. Kunwar<sup>2</sup>, N. Kurahashi<sup>48</sup>, T. Kuwabara<sup>43</sup>, A. Kyriacou<sup>41</sup>, M. Labare<sup>35</sup>, J. L. Lanfranchi<sup>9</sup>, M. J. Larson<sup>4</sup>, F. Lauber<sup>20</sup>, K. Leonard<sup>27</sup>, M. Lesiak-Bzdak<sup>46</sup>, M. Leuermann<sup>11</sup>, Q. R. Liu<sup>27</sup>, C. J. Lozano Mariscal<sup>29</sup>, L. Lu<sup>43</sup>, J. Lünemann<sup>30</sup>, W. Luszczak<sup>27</sup>, J. Madsen<sup>49</sup>, G. Maggi<sup>30</sup>, K. B. M. Mahn<sup>33</sup>, S. Mancina<sup>27</sup>, R. Maruyama<sup>50</sup>, K. Mase<sup>43</sup>, R. Maunu<sup>22</sup>, K. Meagher<sup>3</sup>, M. Medici<sup>4</sup>, M. Meier<sup>25</sup>, T. Menne<sup>25</sup>, G. Merino<sup>27</sup>, T. Meures<sup>3</sup>, S. Miarecki<sup>16,24</sup>, J. Micallef<sup>33</sup>, G. Momenté<sup>15</sup>, T. Montaruli<sup>6</sup>, R. W. Moore<sup>13</sup>, M. Moulai<sup>10</sup>, R. Nahnhauer<sup>2</sup>, P. Nakarmi<sup>47</sup>, U. Naumann<sup>20</sup>, G. Neer<sup>33</sup>, H. Niederhausen<sup>46</sup>, S. C. Nowicki<sup>13</sup>, D. R. Nygren<sup>24</sup>, A. Obertacke Pollmann<sup>20</sup>, A. Olivas<sup>22</sup>, A. O'Murchadha<sup>3</sup>, E. O'Sullivan<sup>5</sup>, T. Palczewski<sup>16,24</sup>, H. Pandya<sup>34</sup>, D. V. Pankova<sup>9</sup>, P. Peiffer<sup>15</sup>, J. A. Pepper<sup>47</sup>, C. Pérez de los Heros<sup>26</sup>, D. Pieloth<sup>25</sup>, E. Pinat<sup>3</sup>, M. Plum<sup>8</sup>, P. B. Price<sup>16</sup>, G. T. Przybylski<sup>24</sup>, C. Raab<sup>3</sup>, L. Rädel<sup>11</sup>, M. Rameez<sup>4</sup>, L. Rauch<sup>2</sup>, K. Rawlins<sup>51</sup>, I. C. Rea<sup>40</sup>, R. Reimann<sup>11</sup>, B. Relethford<sup>48</sup>, M. Relich<sup>43</sup>, E. Resconi<sup>40</sup>, W. Rhode<sup>25</sup>, M. Richman<sup>48</sup>, S. Robertson<sup>41</sup>, M. Rongen<sup>11</sup>, C. Rott<sup>37</sup>, T. Ruhe<sup>25</sup>, D. Ryckbosch<sup>35</sup>, D. Rysewyk<sup>33</sup>, I. Safa<sup>27</sup>, T. Sälzer<sup>11</sup>, S. E. Sanchez Herrera<sup>13</sup>, A. Sandrock<sup>25</sup>, J. Sandroos<sup>15</sup>, M. Santander<sup>47</sup>, S. Sarkar<sup>4,52</sup>, S. Sarkar<sup>13</sup>, K. Satalecka<sup>2</sup>, P. Schlunder<sup>25</sup>, T. Schmidt<sup>22</sup>, A. Schneider<sup>27</sup>, S. Schoenen<sup>11</sup>, S. Schöneberg<sup>19</sup>, L. Schumacher<sup>11</sup>, S. Sclafani<sup>48</sup>, D. Seckel<sup>34</sup>, S. Seunarine<sup>49</sup>, J. Soedingrekso<sup>25</sup>, D. Soldin<sup>34</sup>, M. Song<sup>22</sup>, G. M. Spiczak<sup>49</sup>, C. Spiering<sup>2</sup>, J. Stachurska<sup>2</sup>, M. Stamatikos<sup>17</sup>, T. Stanev<sup>34</sup>, A. Stasik<sup>2</sup>, R. Stein<sup>2</sup>, J. Stettner<sup>11</sup>, A. Steuer<sup>15</sup>, T. Stezelberger<sup>24</sup>, R. G. Stokstad<sup>24</sup>, A. Stößl<sup>43</sup>, N. L. Strotjohann<sup>2</sup>, T. Stuttard<sup>4</sup>, G. W. Sullivan<sup>22</sup>, M. Sutherland<sup>17</sup>, I. Taboada<sup>32</sup>, J. Tatar<sup>16,24</sup>, F. Tenholt<sup>19</sup>, S. Ter-Antonyan<sup>38</sup>, A. Terliuk<sup>2</sup>, S. Tilav<sup>34</sup>, P. A. Toale<sup>47</sup>, M. N. Tobin<sup>27</sup>, C. Tönnis<sup>37</sup>, S. Toscano<sup>30</sup>, D. Tosi<sup>27</sup>, M. Tselengidou<sup>7</sup>, C. F. Tung<sup>32</sup>, A. Turcati<sup>40</sup>, C. F. Turley<sup>9</sup>, B. Ty<sup>27</sup>, E. Unger<sup>26</sup>, M. Usner<sup>2</sup>, J. Vandenbroucke<sup>27</sup>, W. Van Driessche<sup>35</sup>, D. van Eijk<sup>27</sup>, N. van Eijndhoven<sup>30</sup>, S. Vanheule<sup>35</sup>, J. van Santen<sup>2</sup>, E. Vogel<sup>11</sup>, M. Vraeghe<sup>35</sup>, C. Walck<sup>5</sup>, A. Wallace<sup>41</sup>, M. Wallraff<sup>11</sup>, F. D. Wandler<sup>13</sup>, N. Wandkowsky<sup>27</sup>, A. Waza<sup>11</sup>, C. Weaver<sup>13</sup>, M. J. Weiss<sup>9</sup>, C. Wendt<sup>27</sup>, J. Werthebach<sup>27</sup>, S. Westerhoff<sup>27</sup>, B. J. Whelan<sup>41</sup>, K. Wiebe<sup>15</sup>, C. H. Wiebusch<sup>11</sup>, L. Wille<sup>27</sup>, D. R. Williams<sup>47</sup>, L. Wills<sup>48</sup>, M. Wolf<sup>27</sup>, J. Wood<sup>27</sup>, T. R. Wood<sup>13</sup>, E. Woolsey<sup>13</sup>, K. Woschnagg<sup>16</sup>, D. L. Xu<sup>27</sup>, X. W. Xu<sup>38</sup>, Y. Xu<sup>46</sup>, J. P. Yanez<sup>13</sup>, G. Yodh<sup>14</sup>, S. Yoshida<sup>43</sup>, and T. Yuan<sup>27</sup>

(IceCube Collaboration)

<sup>1</sup> Dept. of Physics and Astronomy, University of Canterbury, Private Bag 4800, Christchurch, New Zealand; [analysis@icecube.wisc.edu](mailto:analysis@icecube.wisc.edu)

<sup>2</sup> DESY, D-15738 Zeuthen, Germany

<sup>3</sup> Université Libre de Bruxelles, Science Faculty CP230, B-1050 Brussels, Belgium

<sup>4</sup> Niels Bohr Institute, University of Copenhagen, DK-2100 Copenhagen, Denmark

<sup>5</sup> Oskar Klein Centre and Dept. of Physics, Stockholm University, SE-10691 Stockholm, Sweden

<sup>6</sup> Département de physique nucléaire et corpusculaire, Université de Genève, CH-1211 Genève, Switzerland

<sup>7</sup> Erlangen Centre for Astroparticle Physics, Friedrich-Alexander-Universität Erlangen-Nürnberg, D-91058 Erlangen, Germany

<sup>8</sup> Department of Physics, Marquette University, Milwaukee, WI 53201, USA

<sup>9</sup> Dept. of Physics, Pennsylvania State University, University Park, PA 16802, USA

<sup>10</sup> Dept. of Physics, Massachusetts Institute of Technology, Cambridge, MA 02139, USA

<sup>11</sup> III. Physikalisches Institut, RWTH Aachen University, D-52056 Aachen, Germany

<sup>12</sup> Physics Department, South Dakota School of Mines and Technology, Rapid City, SD 57701, USA

<sup>13</sup> Dept. of Physics, University of Alberta, Edmonton, Alberta, T6G 2E1, Canada

<sup>14</sup> Dept. of Physics and Astronomy, University of California, Irvine, CA 92697, USA

<sup>15</sup> Institute of Physics, University of Mainz, Staudinger Weg 7, D-55099 Mainz, Germany

<sup>16</sup> Dept. of Physics, University of California, Berkeley, CA 94720, USA

<sup>17</sup> Dept. of Physics and Center for Cosmology and Astro-Particle Physics, Ohio State University, Columbus, OH 43210, USA

<sup>18</sup> Dept. of Astronomy, Ohio State University, Columbus, OH 43210, USA

<sup>19</sup> Fakultät für Physik & Astronomie, Ruhr-Universität Bochum, D-44780 Bochum, Germany

- <sup>20</sup> Dept. of Physics, University of Wuppertal, D-42119 Wuppertal, Germany
- <sup>21</sup> Dept. of Physics and Astronomy, University of Rochester, Rochester, NY 14627, USA
- <sup>22</sup> Dept. of Physics, University of Maryland, College Park, MD 20742, USA
- <sup>23</sup> Dept. of Physics and Astronomy, University of Kansas, Lawrence, KS 66045, USA
- <sup>24</sup> Lawrence Berkeley National Laboratory, Berkeley, CA 94720, USA
- <sup>25</sup> Dept. of Physics, TU Dortmund University, D-44221 Dortmund, Germany
- <sup>26</sup> Dept. of Physics and Astronomy, Uppsala University, Box 516, SE-75120 Uppsala, Sweden
- <sup>27</sup> Dept. of Physics and Wisconsin IceCube Particle Astrophysics Center, University of Wisconsin, Madison, WI 53706, USA
- <sup>28</sup> SNOLAB, 1039 Regional Road 24, Creighton Mine 9, Lively, ON, P3Y 1N2, Canada
- <sup>29</sup> Institut für Kernphysik, Westfälische Wilhelms-Universität Münster, D-48149 Münster, Germany
- <sup>30</sup> Vrije Universiteit Brussel (VUB), Dienst ELEM, B-1050 Brussels, Belgium
- <sup>31</sup> Dept. of Astronomy and Astrophysics, Pennsylvania State University, University Park, PA 16802, USA
- <sup>32</sup> School of Physics and Center for Relativistic Astrophysics, Georgia Institute of Technology, Atlanta, GA 30332, USA
- <sup>33</sup> Dept. of Physics and Astronomy, Michigan State University, East Lansing, MI 48824, USA
- <sup>34</sup> Bartol Research Institute and Dept. of Physics and Astronomy, University of Delaware, Newark, DE 19716, USA
- <sup>35</sup> Dept. of Physics and Astronomy, University of Gent, B-9000 Gent, Belgium
- <sup>36</sup> Institut für Physik, Humboldt-Universität zu Berlin, D-12489 Berlin, Germany
- <sup>37</sup> Dept. of Physics, Sungkyunkwan University, Suwon 440-746, Republic of Korea
- <sup>38</sup> Dept. of Physics, Southern University, Baton Rouge, LA 70813, USA
- <sup>39</sup> Dept. of Astronomy, University of Wisconsin, Madison, WI 53706, USA
- <sup>40</sup> Physik-department, Technische Universität München, D-85748 Garching, Germany
- <sup>41</sup> Department of Physics, University of Adelaide, Adelaide, 5005, Australia
- <sup>42</sup> Earthquake Research Institute, University of Tokyo, Bunkyo, Tokyo 113-0032, Japan
- <sup>43</sup> Dept. of Physics and Institute for Global Prominent Research, Chiba University, Chiba 263-8522, Japan
- <sup>44</sup> CTPS, Clark-Atlanta University, Atlanta, GA 30314, USA
- <sup>45</sup> Dept. of Physics, University of Texas at Arlington, 502 Yates St., Science Hall Rm 108, Box 19059, Arlington, TX 76019, USA
- <sup>46</sup> Dept. of Physics and Astronomy, Stony Brook University, Stony Brook, NY 11794-3800, USA
- <sup>47</sup> Dept. of Physics and Astronomy, University of Alabama, Tuscaloosa, AL 35487, USA
- <sup>48</sup> Dept. of Physics, Drexel University, 3141 Chestnut Street, Philadelphia, PA 19104, USA
- <sup>49</sup> Dept. of Physics, University of Wisconsin, River Falls, WI 54022, USA
- <sup>50</sup> Dept. of Physics, Yale University, New Haven, CT 06520, USA
- <sup>51</sup> Dept. of Physics and Astronomy, University of Alaska Anchorage, 3211 Providence Dr., Anchorage, AK 99508, USA
- <sup>52</sup> Dept. of Physics, University of Oxford, 1 Keble Road, Oxford OX1 3NP, UK

Received 2017 December 18; revised 2018 February 27; accepted 2018 March 5; published 2018 April 23

## Abstract

We present a search for coincidence between IceCube TeV neutrinos and fast radio bursts (FRBs). During the search period from 2010 May 31 to 2016 May 12, a total of 29 FRBs with 13 unique locations have been detected in the whole sky. An unbinned maximum likelihood method was used to search for spatial and temporal coincidence between neutrinos and FRBs in expanding time windows, in both the northern and southern hemispheres. No significant correlation was found in six years of IceCube data. Therefore, we set upper limits on neutrino fluence emitted by FRBs as a function of time window duration. We set the most stringent limit obtained to date on neutrino fluence from FRBs with an  $E^{-2}$  energy spectrum assumed, which is  $0.0021 \text{ GeV cm}^{-2}$  per burst for emission timescales up to  $\sim 10^2$  s from the northern hemisphere stacking search.

**Key words:** astroparticle physics – cosmic rays – elementary particles – neutrinos – radiation mechanisms: non-thermal

## 1. Introduction

Fast radio bursts (FRBs) are a new class of astrophysical phenomenon characterized by bright broadband radio emission lasting only a few milliseconds. Since the first FRB discovered in 2007 in archival data from the Parkes Radio Telescope (Lorimer et al. 2007), more than 20 FRBs have been detected by a total of five observatories (Spitler et al. 2014; Masui et al. 2015; Bannister et al. 2017; Caleb et al. 2017). This rules out the hypothesis of an instrumental or terrestrial origin of these phenomena. The number of FRBs detected together with the duration and solid angle searched implies an all-sky FRB occurrence rate of a few thousand per day (Thornton et al. 2013; Spitler et al. 2014), which is consistent with 10% of the core-collapse supernova rate (Murase et al. 2016). The burst durations suggest that FRB progenitors are very compact, with light-transit distances on the order of hundreds of kilometers. The dispersion measures—the time delay of lower frequency signal components, which is proportional to the column density of free electrons along the line of sight—of the detected FRBs

are significantly greater than those the Milky Way alone could provide (Cordes et al. 2016), and the majority of sources have been detected at high Galactic latitudes, indicating extragalactic origin. The distances of the FRBs extracted from their dispersion measures, however, are only upper limits, and precise measurements are yet to be determined (most likely from multi-wavelength observations).

The nature of FRBs is still under heated debate, and a multitude of models have been proposed for the FRB progenitors, the majority of which involve strong magnetic fields and leptonic acceleration. Some models predict millisecond radio bursts from cataclysmic events such as dying stars (Falcke & Rezzolla 2014), neutron star mergers (Totani 2013), or evaporating black holes (Rees 1977). In 2015, 16 additional bursts were detected from the direction of FRB 121102 (Spitler et al. 2014; Scholz et al. 2016), spaced out non-periodically by timescales ranging from seconds to days. This indicates that the cataclysmic scenario is not true at least for this repeating FRB. A multi-wavelength follow-up campaign identified this FRB’s host dwarf galaxy at a distance of  $\sim 1$  Gpc (Chatterjee et al. 2017). It

is unclear whether FRB 121102 is representative of FRBs as a source class or if repetitions are possible for only a sub-class of FRBs.

While leptonic acceleration is typically the default assumption for FRB emission in most models, hadronic acceleration is also possible in the associated regions of the progenitors, which would lead to the production of high-energy cosmic rays and neutrinos (Li et al. 2014). It has been proposed that cosmological FRBs could be linked to exotic phenomena such as oscillations of superconducting cosmic strings (Ye et al. 2017), and some authors predict that such cosmic strings could also produce ultra-high-energy cosmic rays and neutrinos from super heavy particle decays (Berezinsky et al. 2009; Lunardini & Sabancilar 2012). Therefore, both multi-wavelength and multi-messenger follow-ups can provide crucial information to help decipher the origin of FRBs. Here, the IceCube telescope offers the opportunity to search for neutrinos correlated with FRBs.

The IceCube Neutrino Observatory consists of 5160 digital optical modules (DOMs) instrumenting one cubic kilometer of Antarctic ice from depths of 1450 to 2450 m at the geographic South Pole (Aartsen et al. 2017e). Charged products of neutrino interactions in the ice create Cherenkov photons, which are observed by the DOMs and allow for the reconstruction of the initial neutrino energy, direction, and interaction type. Charged-current muon neutrino interactions create muons, which travel along straight paths in the ice, resulting in events with directional resolution  $\lesssim 1^\circ$  at energies above 1 TeV (Maunu 2016). The detector—fully installed since 2010—collects data from the whole sky with an up-time higher than 99% per year, enabling real-time alerts to other instruments and analysis of archival data as a follow-up to interesting signals detected by other observatories.

IceCube has discovered a diffuse astrophysical neutrino flux between 10 TeV and 2.6 PeV in deposited energy (Aartsen et al. 2013a, 2013b, 2014, 2015a, 2015c, 2016a). The arrival directions of these neutrinos are consistent with an isotropic distribution, indicating that a majority of them have originated from extragalactic sources. Although tau neutrinos are yet to be identified among the observed flux (Aartsen et al. 2016b), the flavor ratio is found to be consistent with  $\nu_e:\nu_\mu:\nu_\tau = 1:1:1$  from analyses that combined multiple data sets (Aartsen et al. 2015b) and with events starting inside the detector for all flavor channels (Aartsen et al. 2015d, 2017d). Having a close-to-equal flavor ratio is another feature of astrophysical neutrinos, which have traversed astronomical distances and hence have reached full mixing (Argüelles et al. 2015; Bustamante et al. 2015). While the astrophysical neutrino flux has been detected in multiple channels with high significance, neither clustering in space or time nor cross correlations to catalogs have been found (Aartsen et al. 2017a). The once promising sources for high-energy neutrinos such as GRBs (Abbasi et al. 2012; Aartsen et al. 2015e, 2017b) and blazars (Aartsen et al. 2017c) have been disfavored as the major contributors to the observed flux. To date, the origin of the astrophysical neutrinos remains a mystery.

In Fahey et al. (2017), an analysis of four FRBs with one year of IceCube data was reported. Here, we present the results of a more sophisticated study—implementing expanding search time windows and an unbinned likelihood method with detailed background modeling—in search of high-energy neutrinos from 29 FRBs using the IceCube Neutrino Observatory. This

paper is structured as follows: Section 2 describes the event sample used. We then discuss the analysis method, search strategies, and background modeling in Section 3. In Section 4, we present the sensitivities and discovery potentials based on the analysis method and search strategies established in Section 3. We then report the final results and their interpretation in Section 5. Finally, we conclude and discuss the future prospects for FRB follow-ups with IceCube in Section 6.

## 2. Event Sample

The data used in this analysis are assembled from muon neutrino candidate events selected in previous analyses in search of prompt neutrino coincidence with gamma-ray bursts (GRBs; Aartsen et al. 2015e, 2017b). It consists of ten data sets: five years of data from the northern hemisphere and five from the southern hemisphere (Table 1). Due to the effects of atmospheric muon contamination, which are strong in the south and negligible in the north, the data samples are constructed in two “hemispheres” separated at a decl. of  $\delta = -5^\circ$ . The northern selection extends to  $-5^\circ$  rather than  $0^\circ$  decl. because there is still sufficient Earth overburden at  $-5^\circ$  for efficient absorption of atmospheric muons.

### 2.1. Northern Data Set

The northern data samples ( $\delta > -5^\circ$ ) cover five years of IceCube operation from 2011 May 13 to 2016 May 12, during which 20 northern FRBs were detected (Table 2): three each from a unique source and 17 bursts from FRB 121102. In the northern hemisphere, the Earth filters out cosmic-ray-induced atmospheric muons, so the data samples consist primarily of atmospheric muon neutrinos with a median energy on the order of 1 TeV. The event rate in the northern hemisphere increases from 3.5 mHz in the first year (Aartsen et al. 2015e) to 6 mHz in later years (Aartsen et al. 2017b), as shown in Figure 1. This year-to-year variation is due largely to two combined effects: first, the initial event selections treat each year of the IceCube data sample independently due to filter and data processing scheme updates in the early years of IceCube operation; second, each data sample was separately optimized for sensitivity to its corresponding set of GRBs.<sup>53</sup>

Within each year, a seasonal variation of the background rate can also be seen (Aartsen et al. 2013c). In the Austral summer, the warming atmosphere expands and increases the average height and mean free path of products from cosmic-ray interactions, allowing pions to more frequently decay into  $\mu + \nu_\mu$  and<sup>54</sup> increasing the overall rate of atmospheric muons and neutrinos in IceCube. The phase of the seasonal variation in the northern sample is the same as that in the southern sample because the northern sample is dominated by events between  $+15^\circ$  and  $-5^\circ$  in decl. (Figure 2), which corresponds to production in the atmosphere at latitudes between  $-60^\circ$  and  $-90^\circ$ .

<sup>53</sup> In the northern data set, the IC86-1 sample was optimized for sensitivity to a stacking search for GRBs. In later years, sensitivity to a max-burst (see Section 3.1) search was instead optimized, accounting for the large year-to-year rate fluctuation between samples IC86-1 and IC86-2 (see Figure 1, Table 1).

<sup>54</sup> IceCube cannot differentiate between neutrinos and anti-neutrinos, so here  $\nu_\mu$  denotes both neutrinos and anti-neutrinos.

**Table 1**  
IceCube Data Sets Analyzed

Northern ( $\delta > -5^\circ$ ) Data	Start Date	End Date	Rate (mHz)	Events	Livetime (days)	$\sigma_{90\%}$
IC86-1	2011 May 13	2012 May 15	3.65	107,612	341.9	2 <sup>0</sup> 13
IC86-2	2012 May 15	2013 May 02	5.50	157,754	332.2	2 <sup>0</sup> 68
IC86-3	2013 May 02	2014 May 06	6.20	193,320	362.2	2 <sup>0</sup> 79
IC86-4	2014 May 06	2015 May 15	6.17	197,311	369.8	2 <sup>0</sup> 79
IC86-5	2015 May 15	2016 May 12	6.07	186,600	356.8	2 <sup>0</sup> 83
Southern ( $\delta < -5^\circ$ ) Data	Start Date	End Date	Rate (mHz)	Events	Livetime (days)	$\sigma_{90\%}$
IC79	2010 May 31	2011 May 13	2.46	67,474	314.6	1 <sup>0</sup> 02
IC86-1	2011 May 13	2012 May 15	1.90	58,982	359.6	1 <sup>0</sup> 10
IC86-2	2012 May 15	2013 May 02	3.18	91,485	328.6	1 <sup>0</sup> 05
IC86-3	2013 May 02	2014 May 06	3.23	100,820	358.6	1 <sup>0</sup> 04
IC86-4	2014 May 06	2015 May 18	1.90	60,500	350.7	1 <sup>0</sup> 04

**Note.** Here, “IC79” indicates the first year of data used in this analysis, when the IceCube array consisted of 79 strings; “IC86-1,” “IC86-2,” etc. denote subsequent years of data from the completed 86-string array. The median angular uncertainty among events in each sample is given as a 90% containment radius ( $\sigma_{90\%}$ ), assuming each event reconstruction has a 2D Gaussian point-spread function. Each individual event is assigned a  $\sigma_{90\%}$  based on characteristics of its directional and energy reconstruction, assuming an  $E^{-2}$  energy spectrum, and we use these same  $\sigma_{90\%}$  for all signal spectra injected (Section 4). Because the event reconstruction becomes more accurate for higher energy events (Aartsen et al. 2017a), the southern data sets have smaller  $\sigma_{90\%}$  as a consequence of harder energy cuts to reduce atmospheric background. Year-to-year variations in event rate and  $\sigma_{90\%}$  are the result of event selection methods aimed to maximize sensitivity independently for each data set’s corresponding set of sources in a previous search for GRBs, as described in Section 2.

**Table 2**  
FRBs in This Analysis

Northern ( $\delta > -5^\circ$ ) FRBs	Time (UTC)	Duration (ms)	R.A.	Decl.	IceCube Data Sample
FRB 110523	2011 May 23 15:06:19.738	1.73	21h 45'	-00°12'	IC86-1
FRB 110703	2011 Jul 03 18:59:40.591	<4.3	23h 30'	-02°52'	IC86-1
FRB 121102 b0	2012 Nov 02 06:47:17.117	3.3	05h 32'	33°05'	IC86-2
FRB 130628	2013 Jun 28 03:58:00.02	<0.05	09h 03'	03°26'	IC86-3
FRB 121102 b1	2015 May 17 17:42:08.712	3.8	05h 32'	33°05'	IC86-4
FRB 121102 b2	2015 May 17 17:51:40.921	3.3	05h 32'	33°05'	IC86-4
FRB 121102 b3	2015 Jun 02 16:38:07.575	4.6	05h 32'	33°05'	IC86-5
FRB 121102 b4	2015 Jun 02 16:47:36.484	8.7	05h 32'	33°05'	IC86-5
FRB 121102 b5	2015 Jun 02 17:49:18.627	2.8	05h 32'	33°05'	IC86-5
FRB 121102 b6	2015 Jun 02 17:49:41.319	6.1	05h 32'	33°05'	IC86-5
FRB 121102 b7	2015 Jun 02 17:50:39.298	6.6	05h 32'	33°05'	IC86-5
FRB 121102 b8	2015 Jun 02 17:53:45.528	6.0	05h 32'	33°05'	IC86-5
FRB 121102 b9	2015 Jun 02 17:56:34.787	8.0	05h 32'	33°05'	IC86-5
FRB 121102 b10	2015 Jun 02 17:57:32.020	3.1	05h 32'	33°05'	IC86-5
FRB 121102 b11	2015 Nov 13 08:32:42.375	6.73	05h 32'	33°05'	IC86-5
FRB 121102 b12	2015 Nov 19 10:44:40.524	6.10	05h 32'	33°05'	IC86-5
FRB 121102 b13	2015 Nov 19 10:51:34.957	6.14	05h 32'	33°05'	IC86-5
FRB 121102 b14	2015 Nov 19 10:58:56.234	4.30	05h 32'	33°05'	IC86-5
FRB 121102 b15	2015 Nov 19 11:05:52.492	5.97	05h 32'	33°05'	IC86-5
FRB 121102 b16	2015 Dec 08 04:54:40.262	2.50	05h 32'	33°05'	IC86-5
Southern ( $\delta < -5^\circ$ ) FRBs	Time (UTC)	Duration (ms)	R.A.	Decl.	IceCube Data Sample
FRB 110220	2011 Feb 20 01:55:48.957	5.6	22h 34'	-12°24'	IC79
FRB 110627	2011 Jun 27 21:33:17.474	<1.4	21h 03'	-44°44'	IC86-1
FRB 120127	2012 Jan 27 08:11:21.723	<1.1	23h 15'	-18°25'	IC86-1
FRB 121002	2012 Oct 02 13:09:18.402	2.1; 3.7	18h 14'	-85°11'	IC86-2
FRB 130626	2013 Jun 26 14:56:00.06	<0.12	16h 27'	-07°27'	IC86-3
FRB 130729	2013 Jul 29 09:01:52.64	<4	13h 41'	-05°59'	IC86-3
FRB 131104	2013 Nov 04 18:04:01.2	<0.64	06h 44'	-51°17'	IC86-3
FRB 140514	2014 May 14 17:14:11.06	2.8	22h 34'	-12°18'	IC86-4
FRB 150418	2015 Apr 18 04:29:05.370	0.8	07h 16'	-19°00'	IC86-4

**Note.** Twenty-nine FRBs are included in this search: in the North, 20 bursts from four unique sources locations, and in the South, nine bursts each with a unique location. For each FRB, arrival time and dispersion-measure-corrected burst duration are provided with R.A. and decl. (J2000), as well as the IceCube data sample being recorded during its detection. For FRB 121102, which has been found to repeat, we label individual bursts with “b0,” “b1,” etc., sorted chronologically by time of detection. FRB 121002 was detected as two bursts separated by  $\sim 1$  ms. It is treated as a single burst in this analysis, but we give both burst durations for completeness.

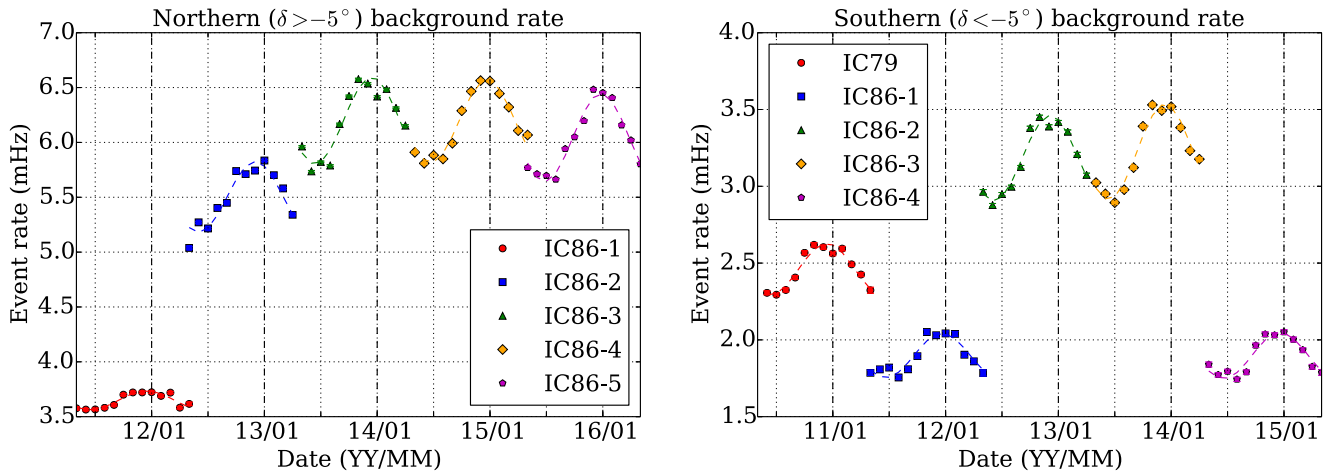


**Figure 1.** Event rates are shown for each data sample, binned by month and fit yearly with one period of a sine function. Year-to-year rate fluctuations reflect changes in event selection methods, not physical changes to the detector, while seasonal variation within each year is the result of the temperature dependence of atmospheric properties that affect atmospheric muon rates. In the northern hemisphere, seasonal variation accounts for a 2%–5% amplitude (mean-to-peak) variation in the year-averaged rate. In the southern hemisphere, the amplitude of this fluctuation is 7%–10%.

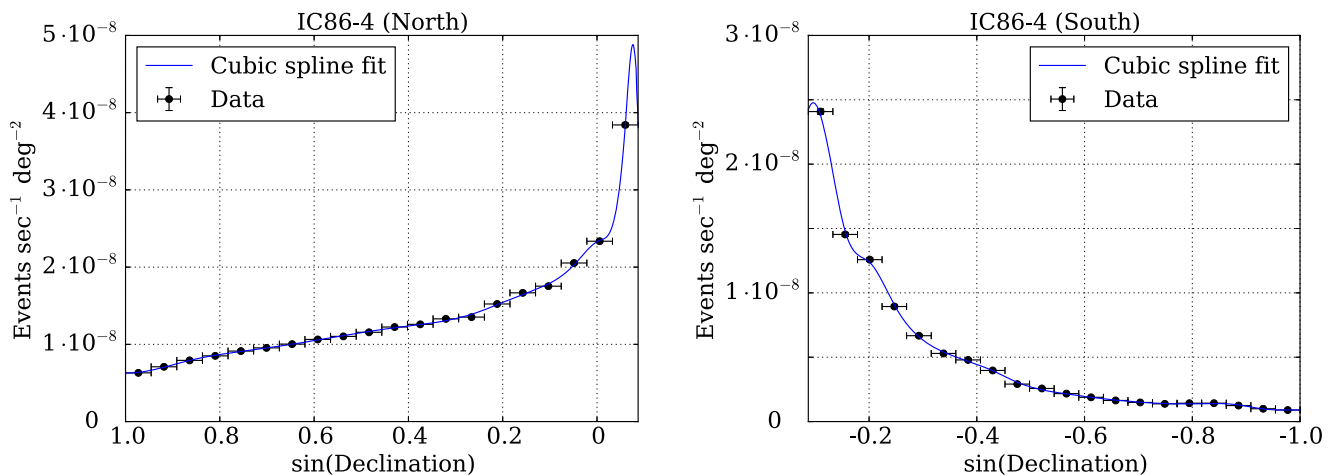


**Figure 2.** The distribution of events in reconstructed decl. is shown for a representative year of off-time data in each hemisphere. Data samples are binned into 20 bins of equal width in  $\sin(\text{decl.})$  and fit with a cubic polynomial spline with endpoints equal to the first and last bin values.

## 2.2. Southern Data Set

The southern data samples ( $\delta < -5^\circ$ ) consist of five years of data from 2010 May 31 to 2015 May 18, during which nine southern FRBs were detected. The year-to-year event rate, 2–3.5 mHz, is lower than that of the northern samples mainly due to a higher energy threshold imposed to reduce background from atmospheric muons and the asymmetric separation of hemispheres, which makes the northern hemisphere  $\sim 20\%$  larger in solid angle than the southern (Aartsen et al. 2017b). The southern samples are dominated by down-going atmospheric muons with median energy on the order of 10 TeV. The effective area of IceCube to neutrino events that pass the event selection can be seen in Figure 3, where the effective area has been determined for the decl. of each FRB in this analysis.

## 3. Analysis Methods

### 3.1. Unbinned Likelihood Method

An unbinned maximum likelihood method is used to search for spatial and temporal coincidence of neutrino events with detected FRBs (Aartsen et al. 2015f). In a given coincidence

window  $\Delta T$  centered on the time of detection of each FRB, the likelihood of observing  $N$  events for an expected  $(n_s + n_b)$  events is

$$\mathcal{L}(N, \{x_i\}; n_s + n_b) = \frac{(n_s + n_b)^N}{N!} \cdot \exp[-(n_s + n_b)] \cdot \prod_{i=1}^N \frac{n_s S(x_i) + n_b B(x_i)}{n_s + n_b} \quad (1)$$

where  $n_s$  and  $n_b$  are the expected number of observed signal and background events,  $x_i$  is the reconstructed direction and estimated angular uncertainty for each event  $i$ ,  $S(x_i)$  is the signal PDF—taken to be a radially symmetric two-dimensional (2D) Gaussian with standard deviation  $\sigma_i$ —evaluated for the angular separation between event  $i$  and the FRB with which it is temporally coincident, and  $B(x_i)$  is the background PDF for the data sample to which event  $i$  belongs evaluated at the decl. of event  $i$ . The uncertainties of the FRB locations are taken into account in  $S(x_i)$ , but they are significantly smaller than the median angular uncertainty of the data. In any time window

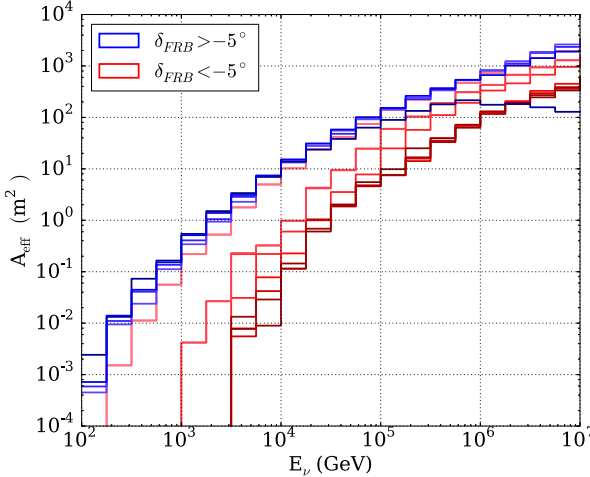


**Figure 3.** Left panel: the effective area of IceCube to muon neutrinos with energies 100 GeV–10 PeV is shown for the event selection applied to this analysis’ data samples. The effective area was calculated for a decl. range  $\Delta\sin(\delta) = 0.04$  centered on the decl. of each FRB using the event selection corresponding each FRB’s respective year of data. In total, 15 unique curves are plotted (three curves are calculated for FRB 121102, one for each year during which it was detected), although they sometimes overlap. Northern- and southern-sky FRBs are plotted in blue and red, respectively, with a color scale for each corresponding to decl. (darker near poles and lighter near the celestial equator). In the southern hemisphere, IceCube’s energy cuts to reduce atmospheric muon contamination result in a smaller effective area at lower energies. In the northern hemisphere, the effective area of IceCube benefits from shielding by the Earth from muons until, at energies above 100 TeV, the increased neutrino-nucleon cross section results in significant absorption of up-going neutrinos. However, because of the decl. of these FRBs, this effect is only easily seen here for FRB 121102 ( $\delta = 33^\circ$ , dark blue curve), for which  $A_{\text{eff}}$  begins to decrease at 1 PeV. Right panel: FRB locations in the sky. The FRB 121102 (red hexagon) has repeated 16 times, and the other FRBs (blue stars) have not been observed to repeat. As FRB 110220 and FRB 140514 were detected only  $9'$  away from each other, one marker has been rotated so that both are visible.

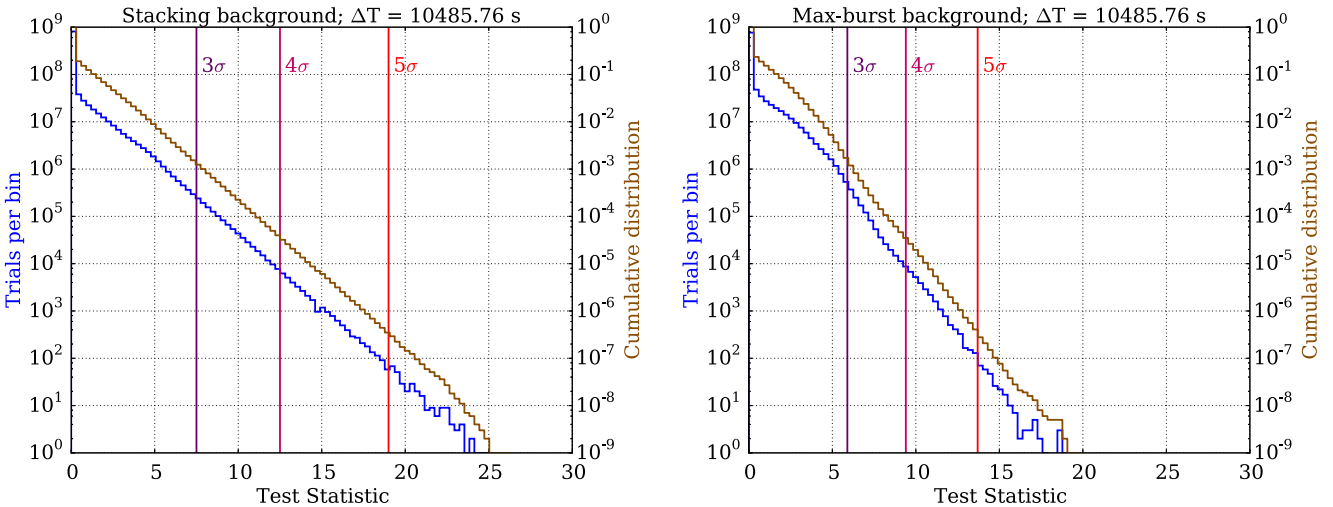


**Figure 4.** TS distributions are shown for  $10^9$  background-only Monte Carlo trials in the southern stacking and max-burst searches at  $\Delta T = 10485.76$  s. Significance thresholds (e.g.,  $5\sigma$ ) are determined using the corresponding  $p$ -value for one tail of a normal distribution. In the low-background regime, each trial is unlikely to contain any spatially coincident events; thus, the majority of trials are more background-like than signal-like, returning a negative TS value. These are rounded to zero, resulting in low-background TS distributions peaked sharply at  $TS = 0$ . As  $\Delta T$  increases, the height of the background TS distribution at  $TS = 0$  approaches 50% of trials as expected.

$\Delta T$ , the  $N$  events are those which IceCube detected within  $\pm \Delta T/2$  of any FRB detection. Before background event rates and PDFs were calculated, *on-time data*—data collected within  $\pm 2$  days of any FRB detection—were removed from the samples until all analysis procedures were determined. The remaining data ( $>1700$  days of data per hemisphere) are considered *off-time data*, which we used to determine background characteristics to prevent artificial bias from affecting the results of our search. Figure 2 shows examples of off-time data distributions for both northern and southern hemispheres.

A generic test statistic (TS) is used in this analysis, defined as the logarithmic ratio of the likelihood of the alternative hypothesis  $\mathcal{L}(N, \{x_i\}; n_s + n_b)$  and that of the null hypothesis

$\mathcal{L}_0(N, \{x_i\}; n_b)$ , which can be written as

$$TS = -n_s + \sum_{i=1}^N \ln \left[ 1 + \frac{n_s S(x_i)}{n_b B(x_i)} \right]. \quad (2)$$

The TS is maximized with respect to  $n_s$  to find the most probable number of signal-like events among  $N$  temporally coincident events.  $n_b$  is calculated by multiplying the time-dependent background rate for each FRB, modeled from off-time data, by  $\Delta T$ .

Two search strategies are implemented based on this TS. The *stacking* search tests the hypothesis that the astrophysical class of FRBs emits neutrinos. In this search,  $n_s$  and  $n_b$  are the total number of expected signal and background events contained in

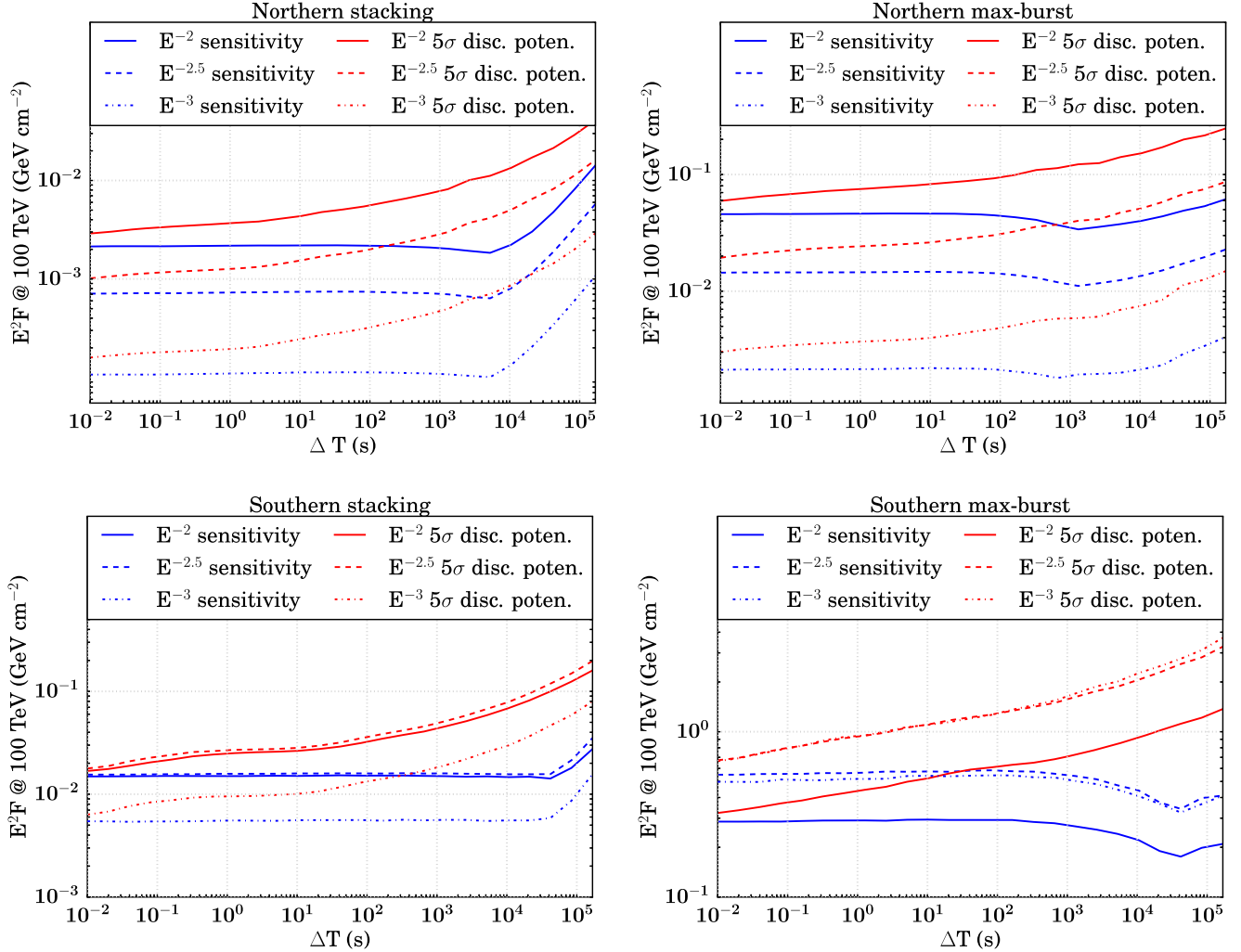


**Figure 5.** Sensitivity and  $5\sigma$  discovery potential (90% confidence level) vs. time-window size are shown for the northern hemisphere stacking, northern max-burst, southern stacking, and southern max-burst searches. The values plotted are  $E^2$  times the time-integrated flux per burst at 100 TeV, for signal spectra of  $E^{-2}$ ,  $E^{-2.5}$ , and  $E^{-3}$ . The central 90% intervals of the expected neutrino energy distributions from these respective spectra are (1.0 TeV, 5.6 PeV), (320 GeV, 320 TeV), and (180 GeV, 32 TeV) for the northern stacking test. In the southern stacking test, these intervals are (10 TeV, 18 PeV), (1.8 TeV, 3.2 PeV), and (560 GeV, 32 TeV).

**Table 3**  
Analysis Results

Northern ( $\delta > -5^\circ$ )	Best-fit TS	Best-fit $n_s$	Most Significant Event ( $t - t_{\text{FRB}}$ , $\Delta\Psi$ )	Pre-trial $p$ (post-trial $p$ )	Optimal $\Delta T$	Coincident FRB
max-burst test	3.90	0.99	(+200.806 s, 2°31)	0.034	655.36 s	FRB 121102 repeater
				0.25		2015 Jun 02 16:38:07.575 UTC
				0.074		FRB 121102 repeater
stacking test	1.41	1.01	(+200.806 s, 2°31)	(0.375)	655.36 s	2015 Jun 02 16:38:07.575 UTC
Southern ( $\delta < -5^\circ$ )	best-fit TS	best-fit $n_s$	most significant event ( $t - t_{\text{FRB}}$ , $\Delta\Psi$ )	pre-trial $p$ (post-trial $p$ )	optimal $\Delta T$	coincident FRB
max-burst test	0.64	0.78	(-16.9 hr, 0°20)	0.412	167772.16 s	FRB 140514
				(0.84)		2014 May 14 17:14:11.06 UTC
				1.0		...
stacking test	0	0	...	(1.0)	...	...

**Note.** Where a most significant TS is found, the timing and directional separation of the event that contributed the most to that TS value are provided. In the southern stacking test, the TS values for all time windows are zero; there is no  $\Delta T$  searched that is more signal-like than background-like.

the time windows of an entire list of FRBs for the hemisphere. One TS value (with its corresponding  $n_s$ ) is returned for an ensemble of  $N$  events that consist of on-time events from all of the bursts. This TS represents the significance of correlation

between the events analyzed and the source class as a whole. The *max-burst* search tests the hypothesis that one or a few bright sources emit neutrinos regardless of source classification. In this search,  $n_s$  and  $n_b$  are evaluated separately for each

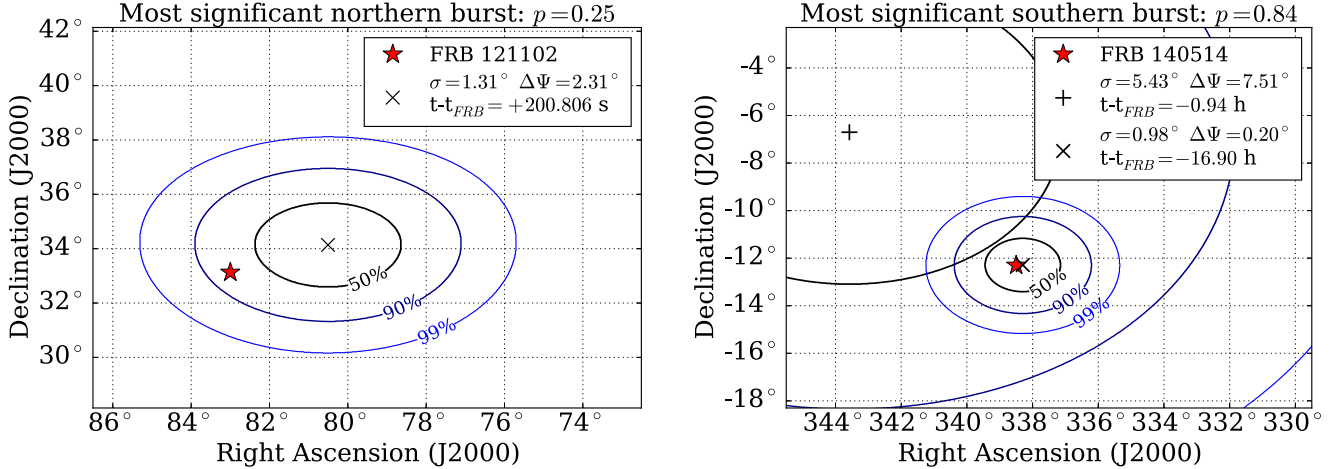


**Figure 6.** Left panel: the most signal-like event in both northern searches was detected 200.806 s after the radio detection of FRB 121102 b3. The directional reconstruction of this event has an angular separation  $\Delta\Psi = 2.31^\circ$  with the FRB and an estimated error  $\sigma = 1.31^\circ$ . Event reconstruction contours are drawn for confidence intervals of 50%, 90%, and 99%, taking the reconstruction as a radially symmetric 2D Gaussian. FRB directional uncertainty ( $\ll 1^\circ$ ) is taken into account in this analysis but not shown for this scale. The post-trial  $p$ -value for this max-burst search is  $p = 0.25$ . Right panel: the most signal-like event in the southern searches was coincident with FRB 140514, with two events' 90%-confidence intervals overlap. One event was detected 0.94 hr before the detection of FRB 140514 with reconstructed angular separation  $\Delta\Psi = 7.51^\circ$  and estimated error  $\sigma = 5.43^\circ$ . The second was detected only in the largest time window, 16.90 hr before the FRB, with  $\Delta\Psi = 0.20^\circ$  and  $\sigma = 0.98^\circ$ . Although this event appears remarkably coincident with the location of FRB 140514, its significance suffers from the high background rate of the time window in which it first appears. Its angular uncertainty is also roughly twice the median angular uncertainty of its background sample, reducing the contribution its signal PDF  $S(x_i)$  has on the TS value. The post-trial  $p$ -value for this max-burst search is  $p = 0.84$ .

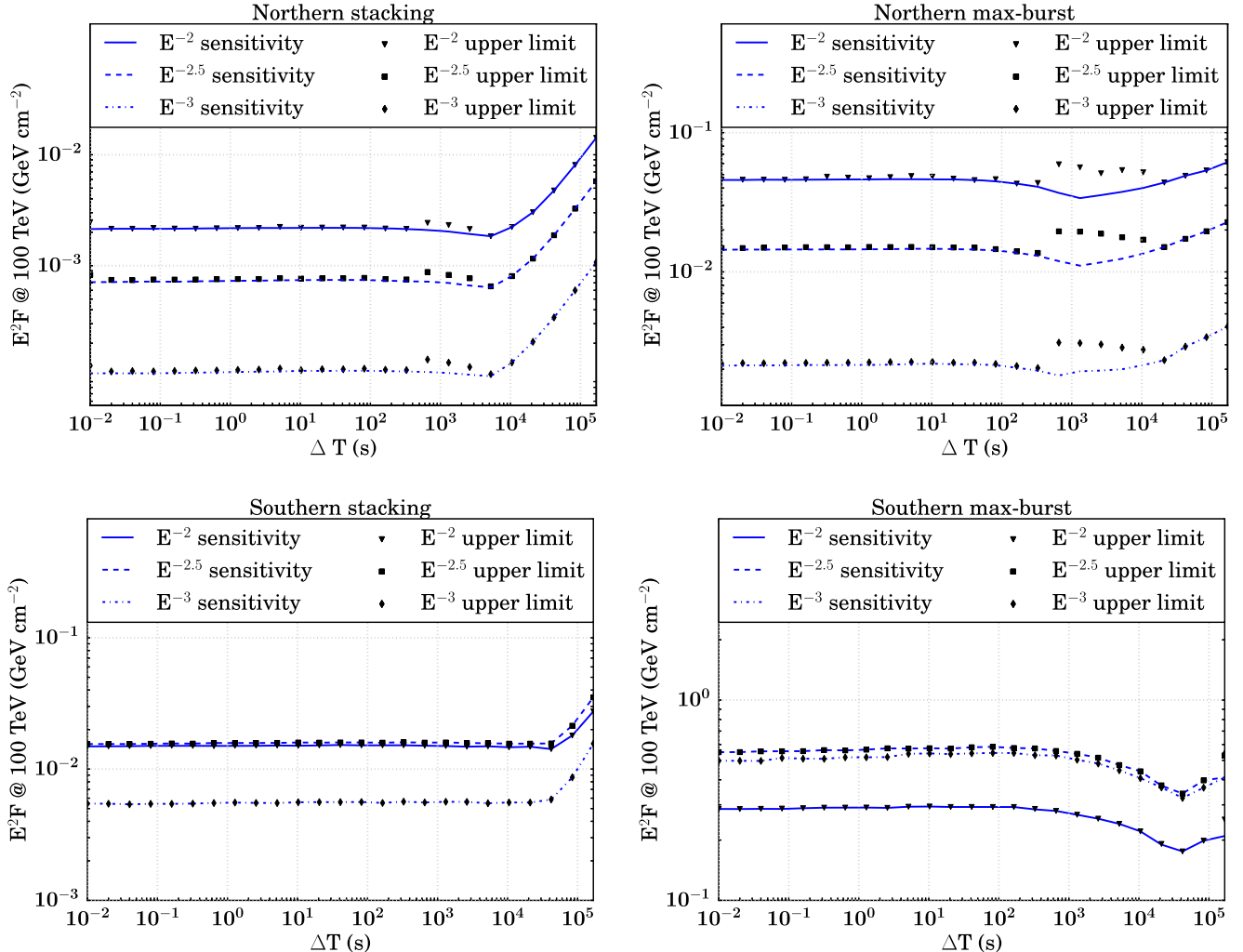


**Figure 7.** Sensitivity and upper limits (90% confidence level) per burst vs.  $\Delta T$  for the stacking and max-burst search in each hemisphere. For the largest  $\Delta T$ 's, in the case that an upper limit fluctuates below the sensitivity, we make the conservative choice to raise the upper limit to the sensitivity value.

**Table 4**  
Individual FRB Neutrino Fluence Upper Limits (90% Confidence)

FRB	Decl.	Fluence Upper Limit (GeV cm <sup>-2</sup> )
FRB 121002	-85°11'	1.16
FRB 131104	-51°17'	1.03
FRB 110627	-44°44'	0.963
FRB 150418	-19°00'	0.331
FRB 120127	-18°25'	0.318
FRB 110220	-12°24'	0.184
FRB 140514	-12°18'	0.192
FRB 130626	-07°27'	0.153
FRB 130729	-05°59'	0.136
FRB 110703	-02°52'	0.0575
FRB 110523	-00°12'	0.0578
FRB 130628	03°26'	0.0643
FRB 121102 b0	33°05'	0.0932
FRB 121102 b1-b2	33°05'	0.0925
FRB 121102 b3-b16	33°05'	0.0919
LOFAR transient	86°22'	0.164

**Note.** The limits have been calculated for each burst individually for the  $\Delta T = 0.01$  s time window and are shown here as  $E^2 F$  assuming an  $E^{-2}$  spectrum. Each burst from FRB 121102 has a limit corresponding to the year of data during which it was detected. As with the limits for the stacking and max-burst tests, these per-burst limits are generally valid even at much longer timescales, until background becomes non-negligible ( $\Delta T > 10^4$  s) or a moderately significant event is detected (e.g.,  $\Delta T > 400$  s for FRB 121102 b3).

FRB. A TS- $n_s$  pair is calculated for each FRB considering only the events coincident with its time window. The most statistically significant of these TS (and its corresponding  $n_s$ ) is returned as the max-burst TS value of the ensemble.

As neutrino emission mechanisms and potential neutrino arrival times relative to the time of radio detection are unknown, we employ a model-independent search using an expanding time window, similar to a previous search for prompt neutrino emission from GRBs by IceCube which found no correlation (Abbasi et al. 2012). Starting with  $\Delta T = 0.01$  s centered on each FRB, we search a series of time windows expanding by factors of two, i.e.,  $\Delta T = 2^j \cdot (0.01$  s) for  $j = 0, 1, 2, \dots, 24$ . We stop expanding at a time window size of 1.94 days (167772.16 s), where the background becomes significant. For the repeating burst FRB 121102 with burst separations less than the largest time window searched, time windows of consecutive bursts stop expanding when otherwise they would overlap. There are also FRBs for which the difference in signal transit durations between electromagnetic waves detected by the radio observatory and neutrinos detected by IceCube, assuming simultaneous emission of the two messengers, is larger than our smallest time window. This is due to the size of the Earth, which has a diameter of 42 light-milliseconds, and the geographical orientation of observatories relative to astronomical events. The largest of these differences is for FRB 121102 b0, for which hypothetically light-simultaneous signal neutrinos would be expected to pass through IceCube 32 milliseconds after its radio signal was detected by Arecibo Observatory. The method of expanding time windows addresses this effect.

In the northern max-burst search, a bright radio burst with a flux of 7.5 Jy detected by the LOFAR radio array (Stewart et al. 2016) was included. This LOFAR burst was detected on 2011 December 24 at 04:33 UTC, near the North Celestial

Pole (R.A. = 22<sup>h</sup>53<sup>m</sup>47<sup>s</sup>.1, decl. = +86°21'46.4'') and lasted ~11 minutes. The burst was not consistent with an FRB, so it was not included in the stacking search, during which some degree of uniformity among the stacked source class was required.

### 3.2. Background Ensembles

For each search method and hemisphere, we simulate  $10^9$  background-only Monte Carlo pseudo-experiments for every  $\Delta T$ . This is done by first finding the seasonal variation-adjusted background rate (from Figure 1) for each FRB in the hemisphere. The product of these rates and  $\Delta T$  gives a set of mean values for the Poisson distributions from which background events will be drawn. In a single trial, the number of events in the time window of each FRB is randomly drawn, and each event is assigned spatial coordinates that are uniform in detector azimuth and have decl. values drawn from the PDFs shown in Figure 2. An angular uncertainty for each event is also randomly assigned from the angular distribution of the off-time data (Maunu 2016). The TS value for the trial is maximized with respect to  $n_s$  and the process is repeated for  $10^9$  trials, forming a TS distribution for the background-only hypothesis.

For example, Figure 4 shows the background-only TS distribution for the southern stacking search at  $\Delta T = 10485.76$  s. Negative TS values are rounded to zero for the purposes of calculating the significance of analysis results. Building a TS distribution in this manner implicitly factors in a trials factor for the number of bursts searched, as increasing the number of sources inflates the TS values of both the analysis result and the background-only distribution. However, there is an additional trials factor when searching in overlapping time windows, so the cross-time-window trials factor must be accounted for when calculating significance values.

For each search, the analysis procedure returns the most optimal time window and the corresponding TS- $n_s$  pair, as determined by the  $p$ -value of the observed TS in the background-only distribution. This  $p$ -value is trials-factor corrected by investigating additional ensembles of background-only trials. For each trial, a set of events is injected for the largest  $\Delta T$  following the background-only procedure described above. Then, for each  $\Delta T$ , a TS value is calculated relative to its corresponding subset of events, which are randomly selected from the total event set. The most significant of these TS values has a  $p$ -value that becomes one background-only pre-trial  $p$ -value. These trials are repeated  $10^5$  times, forming a pre-trial  $p$ -value distribution. The position of the pre-trial  $p$ -value from the search on on-time data in this distribution determines its post-trial  $p$ -value.

## 4. Sensitivity

The sensitivity and discovery potential are calculated by injecting signal events following an assumed unbroken power-law energy spectrum ( $E^{-2}$ ,  $E^{-2.5}$ , and  $E^{-3}$ ) on top of injected background events. The injected signal fluence (time-integrated flux, denoted as  $F$ ) is found, which yields a certain probability of obtaining a certain significance in the background-only TS distribution (Neyman 1937; Aartsen et al. 2017b). Specifically, sensitivity and discovery potential are defined as the minimum signal fluences required to surpass, respectively, the median in 90% of the trials and the  $5\sigma$  point in 90% of the trials. Figure 5 shows the sensitivities and  $5\sigma$  discovery potentials for both

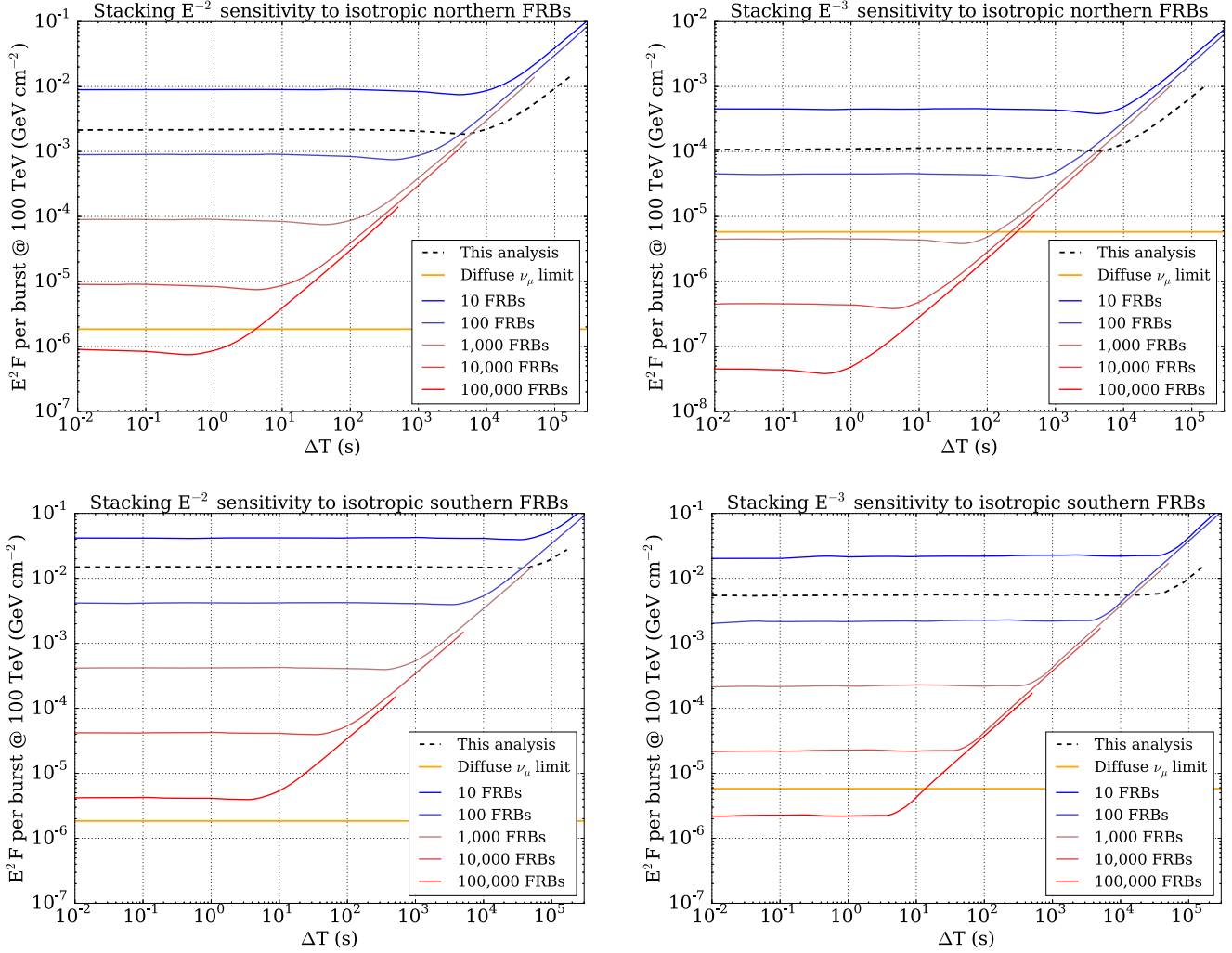


**Figure 8.** Sensitivity vs.  $\Delta T$  for two emission spectra,  $E^{-2}$  and  $E^{-3}$ , in each hemisphere for source list sizes ranging from 10 to 100,000 FRBs, is shown. The stacking sensitivity of FRBs relies on the number and locations of sources detected. Because the list of detected FRBs is expected to grow exponentially in the coming years and without significant directional bias, the per-burst sensitivity to an isotropic hemisphere of FRBs has been calculated for a range of source list sizes. The respective stacking sensitivities from this analysis are overlaid for comparison, with total fluence divided by the number of sources—9 in the south, 20 in the north—for *per-burst* fluence. These sensitivities outperform the expected sensitivity to an isotropic sky because the FRBs in this analysis were of higher-than-isotropic decl. on average. As our background rates peak at the horizon, the rate of coincident background events in stacking trials was lower than what would be expected from an isotropic distribution of FRBs as well. This lowers the baseline for the stacking sensitivity curve and moves the up-turn at large  $\Delta T$  to the right, as shown by the crossover near  $10^4$  s in each plot. For comparison, the limits set by constraining the total all-sky FRB fluence to be less than or equal to IceCube’s astrophysical  $\nu_\mu$  flux are provided, assuming an FRB occurrence rate of  $3000 \text{ sky}^{-1} \text{ day}^{-1}$ . With data optimized specifically for sensitivity to FRBs and an orders-of-magnitude larger FRB source list, we expect future limits to improve upon those set by IceCube’s diffuse astrophysical neutrino flux.

hemispheres and search strategies. The searches in the northern hemisphere are roughly an order of magnitude more sensitive than those in the south, because of the differences in effective area as described in Section 2.

At  $\Delta T = 0.01$  s, we expect fewer than 0.001 background events all-hemisphere per trial in each search. As a result, the median background-only TS value is zero for all  $\Delta T$  until it becomes more probable than not that a background event is injected near an FRB location, resulting in a non-zero TS value. In general, the sensitivity remains constant in a  $\Delta T$  range that is relatively background-free and transitions to a monotonically increasing function in background-dominated  $\Delta T$ . We still search all of these low-background  $\Delta T$  because the discovery potential increases even in the small background regime (Figure 5).

As a result of our methodology, there is a point in the background transition region where the sensitivity fluence appears to improve. Where the median of the background TS

distribution is zero, the 90% sensitivity threshold for signal injection remains constant. But when  $\Delta T$  is growing, there are more background events in each trial, which can give rise to non-zero TS values; thus, the injected fluence necessary to meet the criteria for sensitivity is less. Once the median background TS value becomes non-zero, the sensitivity increases as expected.

## 5. Results

After correcting for trials factors induced by 25 overlapping time windows searched, no significant correlation between neutrino events and FRBs is found (nor with the LOFAR burst). The most significant pre-trial  $p$ -value ( $p = 0.034$ ) is found in the northern max-burst search at  $\Delta T = 655.36$  s, with best-fit TS and  $n_s$  of 3.90 and 0.99, respectively. The post-trial  $p$ -value for this search is  $p = 0.25$ . In the same  $\Delta T$ , the northern stacking search returned a best-fit TS and  $n_s$  of 1.41

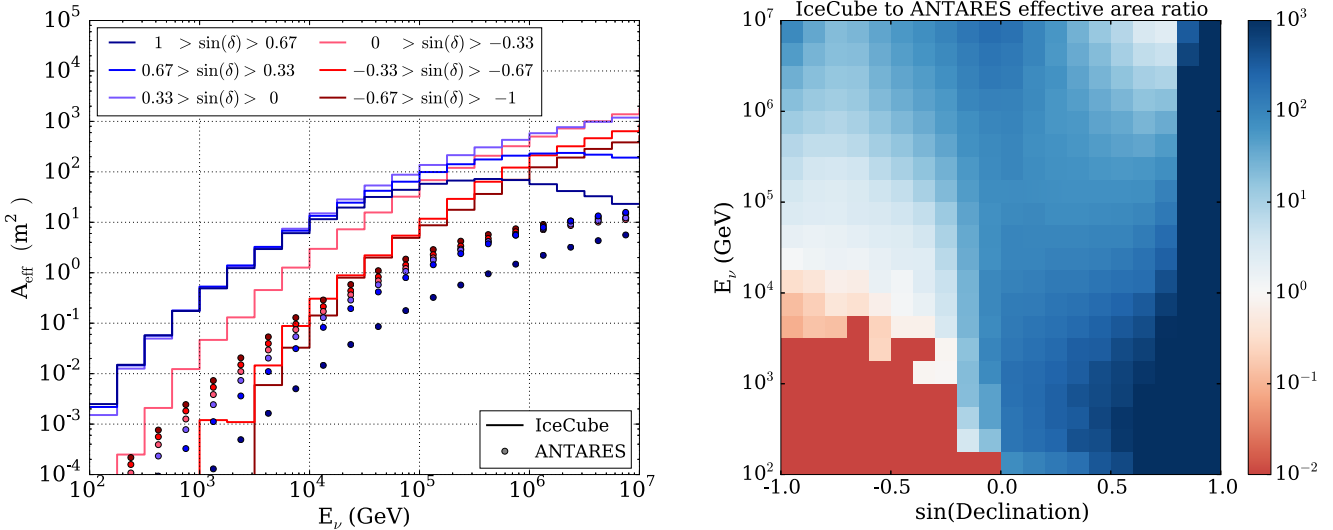


**Figure 9.** Left panel: the effective area of IceCube to muon neutrinos with energies 100 GeV–10 PeV is shown for the event selection applied to this analysis’ data samples. For comparison, the effective area of the ANTARES observatory’s point-source event selection is shown over the same range (circles). Below 1 TeV, the effective area of ANTARES is greater for most of the southern sky and that of IceCube dominates in the north. Above 50 TeV, IceCube’s effective area dominates in all decl. in the energy range for which data are available. Right panel: a 2D plot shows the ratio of the effective areas of IceCube to ANTARES over energy and decl., with a bin-width of 0.1 in  $\sin(\delta)$  and bin-height equal to one-quarter of a decade in energy. Where ANTARES provides a non-zero effective area but IceCube’s is equal to zero for this event selection, the ratio plotted is the scale minimum  $10^{-2}$ ; likewise, where the converse is true, the ratio plotted is the scale maximum  $10^3$ .

and 1.01, respectively, corresponding to a pre-trial  $p$ -value  $p = 0.074$  and post-trial  $p$ -value  $p = 0.375$ . The most signal-like event for both searches occurred 200.806 s after FRB 121102 b3, with an angular separation of  $2.31^\circ$  and estimated angular uncertainty of  $1.31^\circ$ .

In the southern hemisphere, the max-burst search returns the most significant pre-trial  $p$ -value ( $p = 0.412$ ) at  $\Delta T = 167772.16$  s with TS and  $n_s$  of 0.64 and 0.78, for a post-trial  $p$ -value of  $p = 0.84$ . In the southern stacking search, no TS value greater than zero was ever obtained for all  $\Delta T$ . Even for the largest  $\Delta T$ , where the southern max-burst search returned a positive TS value at one FRB, the order-of-magnitude increase in background for nine FRBs stacked sufficiently diminished the significance of the events. Analysis results are summarized in Table 3, and sky maps of the events that contributed the most to the results of each hemisphere are shown in Figure 6.

To set upper limits on the neutrino emission from FRBs, we use the same method that determines sensitivity, using the observed TS rather than the background-only median as a significance threshold. For most  $\Delta T$ , both the background median and analysis result TS values are zero, resulting in an upper limit equal to the sensitivity (Figure 7). The northern stacking search returned the most constraining 90% confidence level upper limit for  $E^{-2}$  neutrino emission from FRBs among all four searches in this analysis,  $E^2 F = 0.0021 \text{ GeV cm}^{-2}$  per burst.

This process has been repeated for each source separately to calculate per-burst upper limits (see Table 4).  $E^{-2}$  fluence upper limits were determined by running background and signal-injection trials for a source list containing only one FRB, repeated for each unique source and for each year in which FRB 121102 was detected.

## 6. Conclusion and Outlook

In a search for muon neutrinos from 29 FRBs detected from 2010 May 31 to 2016 May 12, no significant correlation has

been found. In both hemispheres, several events were found to be spatially coincident with some FRBs but also consistent with background.

Therefore, we set upper limits on neutrino emission from FRBs as a function of time window searched. For an  $E^{-2}$  energy spectrum, the most stringent limit on neutrino fluence per burst is  $E^2 F = 0.0021 \text{ GeV cm}^{-2}$ , obtained from the shortest time window (10 ms) in the northern stacking search. This limit is much improved in comparison to a previous search with only one year of IceCube data and using a binned likelihood method (Fahey et al. 2017). The limits set in this paper are also the most constraining ones on neutrinos from FRBs for neutrino energies above 1 TeV.

At the moment, we can set even more constraining limits on high-energy neutrino emission from FRBs using IceCube’s astrophysical  $\nu_\mu$  flux measurement (Aartsen et al. 2016a), assuming the current catalog of detected FRBs is representative of a homogeneous source class. Using an estimated all-sky FRB occurrence rate of  $3000 \text{ sky}^{-1} \text{ day}^{-1}$  (Macquart & Ekers 2018), the  $\nu_\mu$  fluence per FRB at 100 TeV cannot exceed  $E^2 F = 1.9 \cdot 10^{-6} \text{ GeV cm}^{-2}$  for an emission spectrum of  $E^{-2}$ ; otherwise, FRBs would contribute more than the entire measured astrophysical  $\nu_\mu$  flux. The astrophysical flux used here is extrapolated from a fit at energies of 194 TeV–7.8 PeV, so it is only a rough estimate of the maximum neutrino emission from FRBs in the energy range this analysis concerns.

With newly operating radio observatories like CHIME (CHIME Scientific Collaboration 2017), we expect on the order of 1000 FRBs to be discovered quasi-isotropically each year, which will improve the sensitivity of IceCube to a follow-up stacking search by orders of magnitude (Figure 8). Future analyses using IceCube data may also benefit from a more inclusive data set, allowing a higher overall rate of muon-like and cascade-like events in exchange for increased sensitivity at  $\Delta T < 1000$  s. Cascade-like events do not contain muons, and as a result provide an angular resolution on the order of  $10^\circ$ . However, a coincident event may still provide potential for

high significance in very short time windows, where background is low. Furthermore, if some sub-class of FRBs is associated with nearby supernovae, MeV-scale neutrinos can be searched in the IceCube supernova stream, which looks for a sudden increase in the overall noise rate of the detector modules (Abbasi et al. 2011).

The ANTARES neutrino observatory is most sensitive in the southern hemisphere, where the majority of FRB sources have been detected to date. Higher FRB detection rate (due to more observation time) from the southern hemisphere also provides ANTARES the opportunities for rapid follow-up observations when FRBs are caught in real time (Petroff et al. 2017). However, we emphasize that IceCube also has excellent sensitivity in much of the southern hemisphere. In Figure 9, we provide a quantitative comparison of the effective areas of the two observatories, which can serve as a useful reference when future FRBs are detected at arbitrary decl. (ANTARES Collaboration 2017, private communication). At energies above 50 TeV, the effective area of IceCube to neutrinos is the highest of any neutrino observatory across the entire ( $4\pi$ ) sky (Figure 9). For  $E_\nu < 50$  TeV, particularly where  $\sin(\delta) < -0.33$ , ANTARES complements IceCube in searches for isotropic transient sources, achieving greater effective area in one-third of the sky. As ANTARES is not located at a pole, the zenith angle of any astrophysical source changes throughout the day; thus, detector overburden and sensitivity are time-dependent. Therefore, the effective areas provided by ANTARES for a given decl. band are the day-averaged values (Adrian-Martinez et al. 2014). A joint stacking analysis between IceCube and ANTARES (Adrian-Martinez et al. 2016a, 2016b) could maximize the sensitivity of neutrino searches from FRBs across the full sky. Furthermore, with the implementation of the expanding time window techniques, IceCube can now follow up on generic fast transients rapidly, enabling monitoring of the transient sky in the neutrino sector (Aartsen et al. 2017f).

The IceCube Collaboration designed, constructed, and now operates the IceCube Neutrino Observatory. Data processing and calibration, Monte Carlo simulations of the detector and of theoretical models, and data analyses were performed by a large number of collaboration members, who also discussed and approved the scientific results presented here. The main authors of this manuscript were S. Fahey, J. Vandenbroucke, and D. L. Xu. It was reviewed by the entire collaboration before publication, and all authors approved the final version of the manuscript.

The authors gratefully acknowledge the support from the following agencies and institutions: USA—U.S. National Science Foundation-Office of Polar Programs, U.S. National Science Foundation-Physics Division, Wisconsin Alumni Research Foundation, Center for High Throughput Computing (CHTC) at the University of Wisconsin-Madison, Open Science Grid (OSG), Extreme Science and Engineering Discovery Environment (XSEDE), U.S. Department of Energy-National Energy Research Scientific Computing Center, Particle astrophysics research computing center at the University of Maryland, Institute for Cyber-Enabled Research at Michigan State University, and Astroparticle physics computational facility at Marquette University; Belgium—Funds for Scientific Research (FRS-FNRS and FWO), FWO Odysseus and Big Science programmes, and Belgian Federal Science Policy Office (Belspo); Germany—Bundesministerium für Bildung und Forschung (BMBF), Deutsche Forschungsgemeinschaft

(DFG) and the German Excellence Initiative, Helmholtz Alliance for Astroparticle Physics (HAP), Initiative and Networking Fund of the Helmholtz Association, Deutsches Elektronen Synchrotron (DESY), and High Performance Computing cluster of the RWTH Aachen; Sweden—Swedish Research Council, Swedish Polar Research Secretariat, Swedish National Infrastructure for Computing (SNIC), and Knut and Alice Wallenberg Foundation; Australia—Australian Research Council; Canada—Natural Sciences and Engineering Research Council of Canada, Calcul Qubec, Compute Ontario, Canada Foundation for Innovation, WestGrid, and Compute Canada; Denmark—Villum Fonden, Danish National Research Foundation (DNRF); New Zealand—Marsden Fund; Japan—Japan Society for Promotion of Science (JSPS) and Institute for Global Prominent Research (IGPR) of Chiba University; Korea—National Research Foundation of Korea (NRF); Switzerland—Swiss National Science Foundation (SNSF).

## References

Aartsen, M. G., Abbasi, R., Abdou, Y., et al. (IceCube Collaboration) 2013a, *Sci*, **342**, 1242856  
 Aartsen, M. G., Abbasi, R., Abdou, Y., et al. (IceCube Collaboration) 2013b, *PhRvL*, **111**, 021103  
 Aartsen, M. G., Abbasi, R., Abdou, Y., et al. (IceCube Collaboration) 2013c, arXiv:1309.7003  
 Aartsen, M. G., Abraham, K., Ackermann, M., et al. (IceCube Collaboration) 2015b, *ApJ*, **809**, 98  
 Aartsen, M. G., Abraham, K., Ackermann, M., et al. (IceCube Collaboration) 2015c, *PhRvL*, **115**, 081102  
 Aartsen, M. G., Abraham, K., Ackermann, M., et al. (IceCube Collaboration) 2016a, *ApJ*, **833**, 3  
 Aartsen, M. G., Abraham, K., Ackermann, M., et al. (IceCube Collaboration) 2016b, *PhRvD*, **93**, 022001  
 Aartsen, M. G., Abraham, K., Ackermann, M., et al. (IceCube Collaboration) 2017a, *ApJ*, **835**, 151  
 Aartsen, M. G., Abraham, K., Ackermann, M., et al. (IceCube Collaboration) 2017c, *ApJ*, **835**, 45  
 Aartsen, M. G., Ackermann, M., Adams, J., et al. (IceCube Collaboration) 2014, *PhRvL*, **113**, 101101  
 Aartsen, M. G., Ackermann, M., Adams, J., et al. (IceCube Collaboration) 2015a, *PhRvD*, **91**, 022001  
 Aartsen, M. G., Ackermann, M., Adams, J., et al. (IceCube Collaboration) 2015d, *PhRvL*, **114**, 171102  
 Aartsen, M. G., Ackermann, M., Adams, J., et al. (IceCube Collaboration) 2015e, *ApJL*, **805**, L5  
 Aartsen, M. G., Ackermann, M., Adams, J., et al. (IceCube Collaboration) 2015f, *ApJL*, **805**, L5  
 Aartsen, M. G., Ackermann, M., Adams, J., et al. (IceCube Collaboration) 2017b, *ApJ*, **843**, 112  
 Aartsen, M. G., Ackermann, M., Adams, J., et al. (IceCube Collaboration) 2017d, arXiv:1710.01191  
 Aartsen, M. G., Ackermann, M., Adams, J., et al. (IceCube Collaboration) 2017e, *JINST*, **12**, P03012  
 Aartsen, M. G., Ackermann, M., Adams, J., et al. (IceCube Collaboration) 2017f, *ApH*, **92**, 30  
 Abbasi, R., Abdou, Y., Abu-Zayyad, T., et al. (IceCube Collaboration) 2011, *A&A*, **535**, A109 [Erratum: 2014, *A&A*, 564, C1]  
 Abbasi, R., Abdou, Y., Abu-Zayyad, T., et al. (IceCube Collaboration) 2012, *Natur*, **484**, 351  
 Adrian-Martinez, S., Albert, A., Andre, M., et al. 2014, *ApJL*, **786**, L5  
 Adrian-Martinez, S., Albert, A., Andre, M., et al. 2016a, *PhRvD*, **93**, 122010  
 Adrian-Martinez, S., Albert, A., Andre, M., et al. 2016b, *ApJ*, **823**, 65  
 Argüelles, C. A., Katori, T., & Salvado, J. 2015, *PhRvL*, **115**, 161303  
 Bannister, K., Shannon, R., Macquart, J., et al. 2017, *ApJL*, **841**, L12  
 Berezhinsky, V., Olum, K. D., Sabancilar, E., & Vilenkin, A. 2009, *PhRvD*, **80**, 023014  
 Bustamante, M., Beacom, J. F., & Winter, W. 2015, *PhRvL*, **115**, 161302  
 Caleb, M., Flynn, C., Bailes, M., et al. 2017, *MNRAS*, **468**, 3746  
 Chatterjee, S., Law, C. J., Wharton, R. S., et al. 2017, *Natur*, **541**, 58  
 CHIME Scientific Collaboration 2017, *ApJ*, **844**, 161

Cordes, J. M., Wharton, R. S., Spitler, L. G., Chatterjee, S., & Wasserman, I. 2016, *ApJ*, submitted (arXiv:1605.05890)

Fahey, S., Kheirandish, A., Vandenbroucke, J., & Xu, D. 2017, *ApJ*, 845, 14

Falcke, H., & Rezzolla, L. 2014, *A&A*, 562, A137

Li, X., Zhou, B., He, H.-N., Fan, Y.-Z., & Wei, D.-M. 2014, *ApJ*, 797, 33

Lorimer, D. R., Bailes, M., McLaughlin, M. A., Narkevic, D. J., & Crawford, F. 2007, *Sci*, 318, 777

Lunardini, C., & Sabancilar, E. 2012, *PhRvD*, 86, 085008

Macquart, J.-P., & Ekers, R. 2018, *MNRAS*, 474, 1900

Masui, K., Lin, H.-H., Sievers, J., et al. 2015, *Natur*, 528, 523

Maunu, R. 2016, PhD thesis, Univ. Maryland, <https://drum.lib.umd.edu/handle/1903/18620>

Murase, K., Kashiyama, K., & Mészáros, P. 2016, *MNRAS*, 461, 1498 [Erratum: 2017, *MNRAS*, 467, 3542]

Neyman, J. 1937, *RSPTA*, A236, 333

Petroff, E., Burke-Spolaor, S., Keane, E. F., et al. 2017, *MNRAS*, 469, 4465

Rees, M. J. 1977, *Natur*, 266, 333

Scholz, P., Spitler, L. G., Hessels, J. W. T., et al. 2016, *ApJ*, 833, 177

Spitler, L. G., Cordes, J. M., Hessels, J. W. T., et al. 2014, *ApJ*, 790, 101

Stewart, A. J., Fender, R. P., Broderick, J. W., et al. 2016, *MNRAS*, 456, 2321

Thornton, D., Stappers, B., Bailes, M., et al. 2013, *Sci*, 341, 53

Totani, T. 2013, *PASJ*, 65, L12

Ye, J., Wang, K., & Cai, Y.-F. 2017, *EPJC*, 77, 720